Acta Materialia 272 (2024) 119915

Contents lists available at ScienceDirect

Acta Materialia

journal homepage: www.elsevier.com/locate/actamat

Diffusion dominant thermal transport in mixed valent $Ba_4Sn_4Se_9$

Wilarachchige D.C.B. Gunatilleke [a], Winnie Wong-Ng [b], Adam J. Biacchi [c], Teiyan Chang [d], Yu-Sheng Chen [d], George S. Nolas [a,*]

[a] Department of Physics, University of South Florida, Tampa, FL 33620, USA
[b] Materials Measurement Science Division, National Institute of Standards and Technology, Gaithersburg, MD 20899, USA
[c] Nanoscale Device Characterization Division, National Institute of Standards and Technology, Gaithersburg, MD 20899, USA
[d] ChemMatCARS, University of Chicago, Argonne, IL 60439, USA

ARTICLE INFO

Keywords:
Complex chalcogenides
Crystal growth
X-ray synchrotron radiation
Thermal conductivity
Thermal diffusion

ABSTRACT

New material developments are of paramount importance from the perspective of developing a fundamental understanding of material properties as well as transitioning from materials to devices. Among the different classes of materials of interest, mixed valence Sn compositions have been known to display technologically important properties and are of interest for the design and synthesis of novel compositions for targeted applications. Herein, we report on electronic, optical and thermal properties of the previously unexplored mixed valence composition $Ba_4Sn_4Se_9$, a material with a direct optical band gap of 2.36 eV. As revealed by single crystal synchrotron X-ray diffraction, $Ba_4Sn_4Se_9$ crystallizes in the orthorhombic space group *Pnma* with a large unit cell comprised of 58 atoms. Heat capacity data reveals a low Debye temperature with many low frequency optic modes. Our low temperature thermal conductivity data and analyses show that thermal diffusion dominates thermal transport above 80 K. Furthermore, high lattice anharmonicity contributes to the very low thermal conductivity. Our results and analyses will motivate further investigations of this as well as other compositions in the Ba-Sn-Se system, as well as other mixed valence chalcogenides for technological applications.

1. Introduction

Discovering and identifying material systems with potential for specific applications of interest is complex. Developing a basic understanding of the physical properties, as well as scattering mechanisms limiting the electronic, thermal, or optical properties of such material systems is of paramount importance. Fundamental investigations have shown that multinary chalcogenides possess properties that have great potential for applications such as thermoelectrics [1–5], thermal barrier coatings [6–9], photovoltaics [10–14] and non-linear optics [15–18], while advances in computational capabilities have greatly increased our ability to search for new materials [19,20]. Despite these extensive studies and achievements, the search for new materials for different applications of interest continues to intensify. In this regard, the exploration, discovery and processing of new classes of materials continues as very few new materials discoveries transition to device development [21,22].

Compositions with mixed valence have long been explored for various important applications of interest [23]. For example, photoluminescence has been observed in compounds with both Eu^{2+} and Eu^{3+} [24,25]. Furthermore, the mixed valence state of Sn has been of particular interest as such compositions result in important material properties [26–28] as well as dopants to induce targeted properties [29]. In addition, lone pair electrons introduced by the mixed valence cations have been reported to result in low thermal conductivity [30–33].

The Ba-Sn-Se ternary system accommodates many different compositions and has been explored experimentally and theoretically [34–38] for compositions such as $Ba_7Sn_3Se_{13}$ [38], Ba_2SnSe_4 [39] and Ba_2SnSe_5 [35] in the search for mixed valence compositions. As reported by Li et al. [34], the Ba-Sn-Se ternary phase stability diagram indicates potential formation of new compositions with possible mixed valency, and thermodynamic stability analyses identified a stable region for formation of potential ternary compositions with a Ba to Sn stoichiometric ratio of 1:1. Moreover, the interactions of lone pair electrons containing *p* states of Sn with the *p* states of Se are of interest for thermoelectric and optoelectronic applications [40]. In this work, we report on the crystal growth and physical properties of a new, previously unexplored polymorph in the Ba-Sn-Se system of compounds with mixed Sn valence.

* Corresponding author.
E-mail address: gnolas@usf.edu (G.S. Nolas).

https://doi.org/10.1016/j.actamat.2024.119915
Received 30 January 2024; Received in revised form 9 April 2024; Accepted 10 April 2024
Available online 13 April 2024

$Ba_4Sn_4Se_9$ crystallizes in the orthorhombic space group *Pnma* and possesses a large unit cell with Sn^{2+} and Sn^{4+} leading to heterogeneous bonding around the barium atoms. Temperature dependent electronic and thermal properties, as well as optical spectroscopy studies, indicate that $Ba_4Sn_4Se_9$ is a wide band gap and low thermal conductivity, κ, material. Our analyses of the thermal properties reveal evidence of thermal diffusion dominating the thermal transport in this material. Our findings reaffirm the interest and potential technological importance for investigating the Ba-Sn-Se ternary material system, with many potential compositions yet to be explored, and will also motivate investigations into the design and processing of other novel mixed valence compositions for targeted technological applications.

2. Experimental procedures

2.1. Sample preparation

The new ternary chalcogenide in the Ba-Sn-Se material system was first observed as a secondary phase in an attempt to grow crystals of $BaSnSe_2$. The synthesis method was then optimized to obtain crystals of $Ba_4Sn_4Se_9$ utilizing direct reaction of appropriate binaries. All synthesis attempts using direct reaction of elements, and metal flux growth, failed to produce crystals of $Ba_4Sn_4Se_9$. To prepare BaSe, a 1:1 stoichiometric mixture of Ba pieces (99.2 %, Alfa Aesar) and Se powder (Alfa Aesar, 99.999 %) was sealed in a silica ampoule under vacuum and heated up to 1073 K at 30 K/h, at which point the heating rate was lowered to 5 K/h and further heated up to 1213 K. After the ampoule with the elemental mixture was at this temperature for 72 h, the furnace was turned off. The synthesized BaSe and commercially available SnSe (Alfa Aesar, 99.999 %) binaries were combined in a 1:1 stoichiometric ratio and ball milled in a planetary ball mill to obtain a homogeneous mixture. The stainless-steel milling jars were assembled inside a glovebox with a nitrogen atmosphere with stainless-steel milling balls to powder mass ratio of 40 to 1. Ball milling was carried out using a gear drive 4-station planetary ball mill (Acros International, model no. PQ-N2) at 425 rpm for 10 min. The powder was then inserted into a silica ampoule and placed in a quartz tube. The quartz tube was sealed under vacuum before being placed in a resistive furnace. It was then heated to 1273 K at a rate of 20 K/h and held at this temperature for 48 h at which point it was slowly cooled to 673 K at 4 K/h. The cooling rate was then increased to 10 K/h to bring the reaction mixture to ambient temperature. Small grey crystals with facet dimensions of less than 1 mm were obtained and used for structure characterization, optical properties measurements and temperature dependent electrical and thermal properties measurements.

2.2. Single crystal synchrotron X-ray diffraction and structure refinement

Single crystal synchrotron X-ray diffraction (XRD) measurements were carried out at NSF's ChemMatCARS, Sector 15 of the Advanced Photon Source, Argonne National Laboratory. Data were collected using a Huber 3-circle diffractometer equipped with a Pilatus3 × 2 M detector at 100 K using an Oxford Cryojet.[1] The ω-angle was set at −180°, κ-angle was set at 0° and 30°, with ϕ-angle scanned over the range of 360° using the shutterless mode of the detector. Data integration was performed with Bruker APEX 3 suite software [41,42]. The reduction of data was conducted with SAINT v.8.38A and SADABS v.2016 programs included in the APEX suite. The structure was solved by direct methods and refined by the full-matrix least-squares [41,42].

[1] Certain trade names and company products are mentioned in the text or identified in illustrations in order to adequately specify the experimental procedures and equipment used. In no case does such identification imply recommendation or endorsement by the National Institute of Standards and Technology.

2.3. Energy dispersive spectroscopy

Energy dispersive spectroscopy (EDS) was performed on several crystals with an Oxford INCA X-Sight 7582 M (INCA software) equipped with a scanning electron microscope (JEOL JSM-6390LV). The empirical formula obtained for the material using EDS results corroborated our structure refinement results.

2.4. Electron localization function calculations

Structural data from our refinement results were used for electron localization function (ELF) calculations performed using the Quantum Espresso package [43] based on self-consistent Kohn-Sham orbitals. Self-consistent field (SCF) calculations were based on the Perdew–Burke-Ernzerhof (PBE) approximation [44,45] with Ba $5s^25p^66s^2$, Sn $4d^{10}5s^25p^2$ and Se $4s^24p^4$ valence configurations considered for projector-augmented waves (PAW) pseudopotentials [46]. A $2 \times 2 \times 2\,k$ mesh, kinetic energy cut- off of 640 eV and energy convergence threshold of 10^{-6} eV was used. Analyses and visualization of the ELF distribution were performed using the Vesta software [47].

2.5. Temperature dependent electrical and thermal property measurements

One of the larger crystals of $Ba_4Sn_4Se_9$ was used for low temperature electrical and thermal properties measurements. Measurement of low temperature transport properties of small crystals of mm scale is a challenging task. A custom-built radiation-shielded vacuum probe [48,49] was used for the measurement and the techniques for mounting the crystals has been previously demonstrated [50–53]. An approximately $0.5 \times 1.5 \times 1.5$ mm^3 crystal was used for measurement of the electrical and thermal properties from 300 K to 20 K with a maximum experimental uncertainty of ±20 % associated with determination of the geometrical dimensions of the crystal. Low-temperature heat capacity, C_p, was measured using the heat capacity option on a commercial Quantum Design Physical Property Measurement System using the thermal N-grease accompanied by appropriate addenda. The maximum experimental uncertainty in the entire temperature range was estimated to be ± 3 %.

2.6. Optical property measurements

Backscattered reflection spectroscopy was performed on a mounted $Ba_4Sn_4Se_9$ single crystal using a Photon IMA hyperspectral microscope equipped with a broadband halogen lamp and CMOS detector (Hamamatsu C13440). The collection efficiency was calibrated with a reflectance standard (Spectralon, Edmund Optics). The band gap was determined by a Tauc plot of the Kubelka-Munk transform. Photoluminescence spectra were collected using a Renishaw InVia Microscope with 514.5 nm Ar^+ laser excitation and emission detection on a 1″ CCD spread off a 1200 lines/mm grating.

3. Results and discussion

3.1. Crystal structure

$Ba_4Sn_4Se_9$ forms in a new, orthorhombic polychalcogenide. Table 1 shows the crystallographic data from synchrotron single-crystal XRD structure refinement. Table 2 provides the atomic coordinates and isotropic atomic displacement parameters, U_{eq}. Table 3 contains the anisotropic displacement parameters, U_{ij}, and Tables S1 and S2 in the *Supplementary Information* provide the selected bond distances and bond angles, respectively.

The crystal structure of $Ba_4Sn_4Se_9$ consists of discrete Sn_4Se_9 units that are connected to each other via Ba atoms forming a 3D network, as shown in Fig. 1(a) and (b). Within each Sn_4Se_9 unit, the Sn atoms have

Table 1
Crystal data and structure refinement.

Empirical formula	$Ba_4Sn_4Se_9$
Formula weight	433.69
Temperature/K	100(2)
Crystal system	Orthorhombic
Space group	*Pnma* (No. 62)
a/Å	12.4751(3)
b/Å	9.2631(2)
c/Å	18.1189(4)
Volume/Å^3	2093.79(8)
Z	4
ρ_{calc}/g cm^{-3}	5.503
μ/mm^{-1}	11.468
F(000)	2920
Crystal size/mm^3	0.025 × 0.015 × 0.01
2Θ range for data collection/°	2.304 to 40.284
Index ranges	$-20 \leq h \leq 20$, $-15 \leq k \leq 15$, $-30 \leq l \leq 30$
Reflections collected	118,607
Independent reflections	5315 [R_{int} = 0.0611, R_{sigma} = 0.0196]
Data/restraints/parameters	5315/0/93
Goodness-of-fit on F^2	1.231
Final R indeces [$I > 2\sigma$ (I)]	R_1 = 0.0181, wR_2 = 0.0436
R indices (all data)	R_1 = 0.0203, wR_2 = 0.0440
Largest diff. peak/hole / e Å^{-3}	1.91/−1.51

Table 2
Atomic coordinates and equivalent isotropic displacement parameters (Å^2) for $Ba_4Sn_4Se_9$. U_{eq} is defined as one third of the trace of the orthogonalized U_{ij} tensor.

	x	*y*	*z*	U_{eq}
Ba(1)	0.81935(2)	0.50040(2)	0.05732(2)	0.00525(3)
Ba(2)	0.83473(2)	0.49683(1)	0.31188(2)	0.00623(3)
Sn(1)	0.58829(2)	0.75	0.38893(2)	0.00461(4)
Sn(2)	0.47782(2)	0.25	0.00524(2)	0.00569(4)
Sn(3)	0.59101(2)	0.25	0.19669(2)	0.00583(4)
Sn(4)	0.56885(2)	0.75	0.19348(2)	0.01029(5)
Se(1)	0.78101(3)	0.75	0.43403(2)	0.00526(6)
Se(2)	0.48904(3)	0.75	0.50882(2)	0.00542(6)
Se(3)	0.56210(2)	0.46771(3)	0.09671(2)	0.00558(4)
Se(4)	0.28407(3)	0.25	0.06359(2)	0.00560(6)
Se(5)	0.80039(3)	0.25	0.18776(2)	0.00583(6)
Se(6)	0.77655(3)	0.75	0.18729(2)	0.00524(6)
Se(7)	0.55612(2)	0.97545(3)	0.31343(2)	0.00655(4)

two types of coordination, the 3-fold $SnSe_3$ (trigonal pyramidal geometry) and the 4-fold $SnSe_4$ (distorted tetrahedral environment). The shortest Sn-Se bond is the tetrahedral bond whereas the Sn-Se bond distances in the trigonal pyramidal geometry are longer, with Sn non-bonding orbitals projecting away from the triangular Se planes as seen in the ELF distribution on the (011) lattice plane (Fig. 2). The Sn_4Se_9 motifs form 2-dimensional layers parallel to the a-c plane. There are two independent Ba sites (Ba(1) and Ba(2)) in the structure, both have a 7-coordination environment to Se as distorted monocapped triangular prisms. Ba (1) has a longer distance to Se (7), 3.7764(3) Å, therefore it can also be viewed as a distorted bicapped triangular prism environment (7 + 1 coordination environment). These coordination environments were also observed in other chalcogenides containing Ba^{2+} cations. Specifically, the Ba-Se distances are similar to those reported for the other compositions, for example in Ba_2SnSe_5 [35], $BaGa_4Se_7$ [54], $Ba_7Sn_3Se_{13}$ [38], $Ba_6Sn_6Se_{13}$ [36] and Ba_2SnSe_4 [39]. As shown in Fig. 3, the SEM/EDS analyses of several crystals were performed and an empirical formula of $Ba_{23.1(2)}Sn_{23.3(2)}Se_{51.2(4)}$ was obtained, corroborating the molecular formula shown in Table 1.

3.2. Heat capacity

The unit cell of the $Ba_4Sn_4Se_9$ crystal structure has 58 atoms. Due to the complexity of the structure arising from the heterogeneous bonding due to mixed valence Sn, low frequency optic modes may exist that can directly affect the thermal properties of $Ba_4Sn_4Se_9$, as observed in other polychalcogenides [55–57]. Moreover, the lattice optic modes may be a significant aspect of the thermal properties due to the complexity of the crystal structure. Hence, to investigate the thermal properties of this material, we first measured the low temperature C_p. As shown in Fig. 4, the Dulong-Petit limit is achieved near 200 K indicating that the majority of acoustic and optic mode frequencies are excited above this temperature. The solid line in the inset of Fig. 4 is a low temperature linear fit to the data of the form, $C_p = \gamma T + \beta T^3$, where the first and second terms represent the Sommerfeld coefficient and the lattice contribution, respectively [58]. Using the lattice contribution from the data fit, $\beta = 1.8$ mJ mol^{-1}K^{-4}, the Debye temperature, θ_D, was determined from the low temperature C_p data using the relation $\theta_D = (12\pi^4 R n_a/5\beta)^{1/3}$, where n_a is the number of atoms per formula unit and R is the universal gas constant. A value of 263 K was thus obtained for θ_D. The density of states at the Fermi level, $N(E_F)$, can be estimated from the relation [58],

$$\gamma = \frac{\pi^2}{3} k_B^2 N(E_F)\left(1 + \lambda_{e-ph}\right), \tag{1}$$

where $\gamma = 3.5$ mJ mol^{-1}K^{-2} from our data fit and λ_{e-ph} is the electron-phonon coupling constant, assumed to be zero as a first approximation. The resulting $N(E_F) = 1.5$ eV^{-1} per formula unit indicates poor electrical conductivity, as expected given the band gap and analyses of the photoluminescence spectrum described below. We further confirmed this by measuring the electrical resistivity, ρ. As shown in Fig. 6, a value of 0.1 Ω m at room temperature was obtained from our four-probe resistivity measurements with an exponential temperature dependence with decreasing temperature, in line with the behavior expected for the band gap of this material. As shown in Fig. 5, the C_p/T^3 vs. T for $Ba_4Sn_4Se_9$ shows deviation from Debye behavior. For a crystalline material such a boson peak typically occurs due to excitation of optic phonons [59]. The peak at 11 K was used to estimate the Einstein temperature, θ_E, of optic modes at $5T_{max}$ to be 55 K. The relatively low value of θ_E obtained points to low-lying optic bands above which low velocity phonons may dominate the thermal transport. Typically, such

Table 3
Anisotropic displacement parameters (Å^2). The anisotropic displacement factor exponent takes the form: $-2p^2[h^2a^*2U_{11} + \ldots + 2\,h\,k\,a^*\,b^*\,U_{12}]$.

	U_{11}	U_{22}	U_{33}	U_{23}	U_{13}	U_{12}
Ba (1)	5.49(6)	4.33(6)	5.92(6)	−0.17 (5)	0.72(4)	−0.12 (4)
Ba (2)	7.92(6)	5.20(6)	5.59(6)	−0.30 (5)	−0.83(4)	1.17(5)
Sn (1)	4.35(9)	5.01(9)	4.47(9)	0	−0.01(7)	0
Sn (2)	5.00(9)	7.55(10)	5.12 (10)	0	0.10(8)	0
Sn (3)	5.71 (10)	5.42(10)	6.36 (10)	0	0.75(8)	0
Sn (4)	5.01 (10)	18.29 (13)	7.57 (11)	0	−0.77(8)	0
Se(1)	4.76 (13)	5.85(13)	5.18 (13)	0	−0.34 (10)	0
Se(2)	4.31 (13)	6.55(13)	5.39 (13)	0	0.39(10)	0
Se(3)	5.00(9)	5.19(9)	6.56(9)	0.04(8)	−0.23(7)	−0.21 (7)
Se(4)	4.60 (13)	5.99(13)	6.21 (13)	0	−0.43 (10)	0
Se(5)	6.41 (13)	5.04(13)	6.04 (14)	0	−0.74 (11)	0
Se(6)	5.31 (13)	5.04(13)	5.38 (13)	0	−0.1(1)	0
Se(7)	6.38(9)	5.91(9)	7.35 (10)	1.47(8)	−0.87(8)	0.02(8)

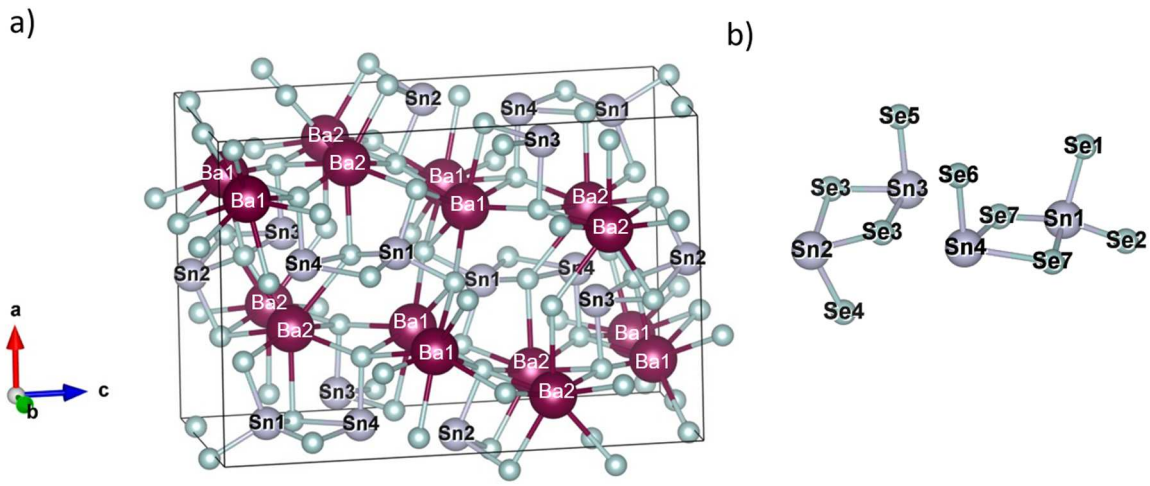

Fig. 1. (a) Crystal structure of $Ba_4Sn_4Se_9$ and (b) Sn_4Se_9 motifs.

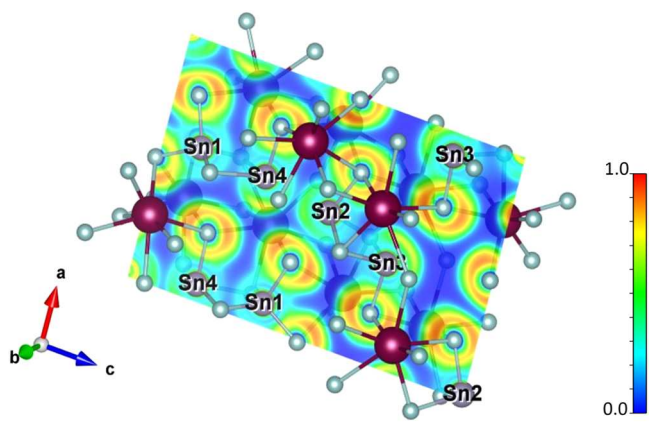

Fig. 2. The ELF distribution of Sn sites on the (011) lattice plane exhibiting lone pair electrons on the Sn2, Sn3 and Sn4 sites.

Einstein-like soft modes are observed in materials with atoms possessing high displacement parameters [49,60–62], however they have also been identified in complex crystal lattices with many atom unit cells [63,64].

3.3. Optical properties

To investigate the optical properties of this previously unascertained material, we performed spectroscopic measurements. From the reflectance spectrum, as shown in Fig. 7, a Tauc plot was constructed (inset to Fig. 7) using the Kubelka-Munk transform of the reflectance and plotting the Kubelka-Munk function, $(F(R)h\nu)^2$, as a function of photon energy, $h\nu$. A good linear fit was obtained with the square of the Kubelka-Munk function for our data, indicating a direct gap of 2.36 eV. The direct photonic electron transition was confirmed using photoluminescence spectroscopy. Broad emission was detected when excited with a 514.5 nm laser, as shown in Fig. 8, with peak emission detected at 611 nm. This wavelength correlates to 2.03 eV, revealing a relatively large Stokes shift of 0.33 eV for optical excitation-induced emission of $Ba_4Sn_4Se_9$. The broadness of the emission suggests multiple weaker underlying transitions due to mid-gap states or more complicated photophysical processes. Notably, negligible photoluminescence was detected when excited with a 532 nm solid state laser, verifying that the optical band gap of 2.36 eV is greater than the energy of these photons (2.03 eV).

3.4. Thermal conductivity

The complex crystal structure of $Ba_4Sn_4Se_9$ may affect the thermal transport of the material due to high lattice anharmonicity. However, as shown in Fig. 9, the very low κ values above 100 K are temperature independent suggesting the existence of another mechanism for heat propagation in addition to phonon transport involving the scattering mechanisms described in a typical phonon-gas model. Compositions with complex crystal structures are known to display diffusion-like transport [65,66]. Furthermore, recent reports on the thermal properties of certain crystalline solids show that diffusion-like thermal transport results in κ values that are relatively temperature independent at higher temperatures [67,68]. In order to investigate the different

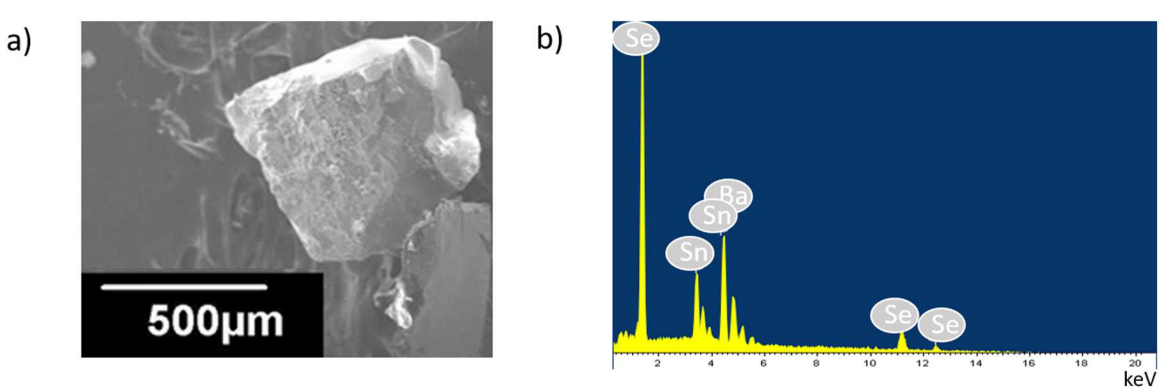

Fig. 3. (a) SEM image of a representative crystal of $Ba_4Sn_4Se_9$ mounted on adhesive carbon tape with conductive copper tape. (b) Representative EDS spectrum obtained for $Ba_4Sn_4Se_9$. Several peaks have been labeled with their corresponding elements.

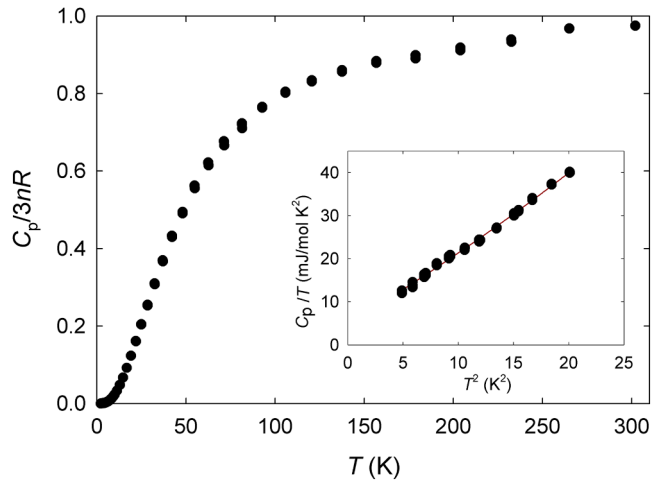

Fig. 4. Low temperature C_p data normalized to the Dulong-Petit limit. The inset shows the Cp/T vs T^2 dependence. The solid line represents a linear fit to the relation $C_p = \gamma T + \beta T^3$.

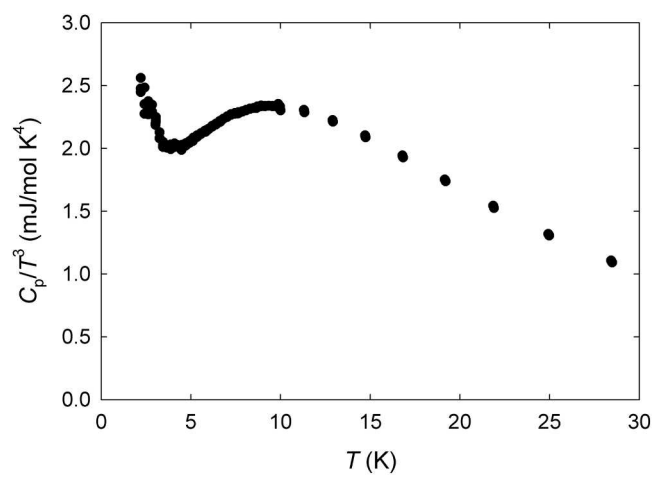

Fig. 5. Cp/T^3 vs T illustrating the deviation from the Debye model.

phonon scattering mechanisms as well as potential contribution to κ from diffusion thermal transport, we utilized a combined phenomenological model that consists of the Debye-Callaway model [69], for lattice thermal conductivity, κ_L, and a diffusion transport model [70], κ_{diff}.

$Ba_4Sn_4Se_9$ possesses relatively low κ over the entire measured temperature range, as shown in Fig. 9. The electronic contribution to κ was deemed to be negligible due to very high ρ values for this wide band gap material, as shown in Fig. 6. In Fig. 9, the solid line is a theoretical fit to the model [69,70]:

$$\kappa = \kappa_L + \kappa_{diff} \tag{2}$$

where,

$$\kappa_{diff} = D\left(\frac{n^{-2/3}k_B}{2\pi^2 v^3}\right)\left(\frac{k_B T}{\hbar}\right)^4 \int_0^{f\theta_D/T} \frac{x^5 e^x}{(e^x-1)^2}dx \tag{3}$$

and

$$\kappa_L = \frac{k_B}{2\pi^2 v}\left(\frac{k_B T}{\hbar}\right)^3 \int_0^{\theta_D/T} \frac{x^4 e^x}{\tau_C^{-1}(e^x-1)^2}dx \tag{4}$$

Here $x = \hbar\omega/k_B T$, ω is the phonon frequency, $\hbar$ is the reduced

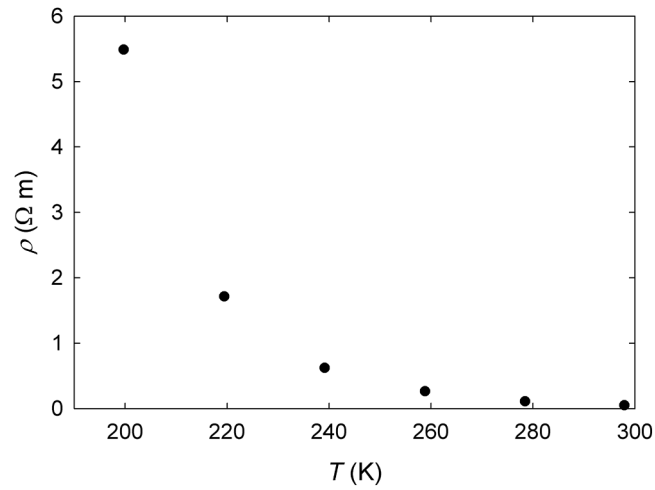

Fig. 6. Temperature dependent ρ data. The ρ was too high to be measured below 200 K.

Planck's constant, υ is the average velocity of sound and n is the number of atoms in the unit cell per unit cell volume. The phonon scattering relaxation time, τ_C^{-1}, is given by,

$$\tau_C^{-1} = \left(\frac{\upsilon}{L} + AT^4x^4 + BT^3\exp\left(\frac{-\theta_D}{3T}\right)x^2\right) \tag{5}$$

where the three terms represent grain boundary scattering, point defect scattering and Umklapp scattering respectively. A, B, D and f are fitting parameters related to the different phonon scattering processes. The fitting parameters were uniquely defined using minimization of the best sequence fit function, as compared to the data. To achieve the best data fit, all three terms related to τ_C^{-1} as well as the expression for κ_{diff} were required. As shown in Fig. 9, the model fits the data very well over the entire measured temperature range yielding fitting parameters of $A = 1.3 \times 10^{-40}$ s^3, $B = 2.9 \times 10^{-16}$ s/K, $\upsilon = 1650$ m/s, $L = 1$ μm, $D = 2.0$ and $f = 1$. With increasing temperature, κ_{diff} starts to dominate the thermal transport. Notably, even though C_p data suggests the existence of low frequency optic modes (Fig. 5), resonance scattering was not deemed to be a major contributor to τ_C from our analyses. The very good fit obtained for the data using only grain boundary scattering, point defect scattering and Umklapp scattering suggests that above 80 K κ_{diff} dominates. Utilizing the B parameter from the theoretical fit to the phenomenological model, the Gruneisen parameter, γ, was estimated to

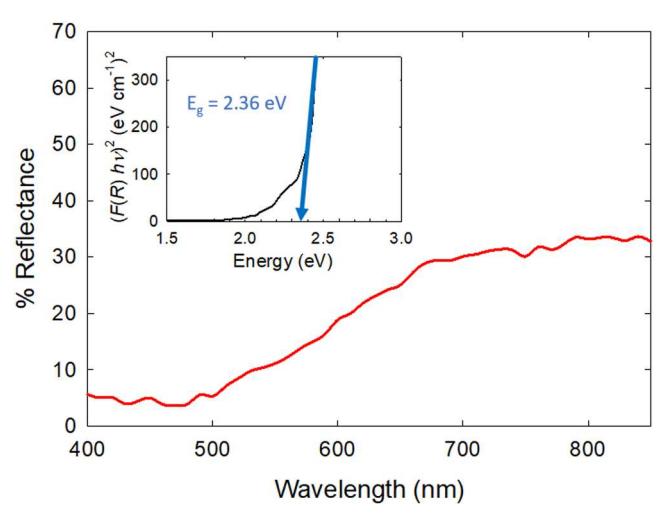

Fig. 7. UV–vis-NIR reflectance spectrum with corresponding Tauc plot of the Kubelka-Munk function indicating a direct band gap of 2.36 eV.

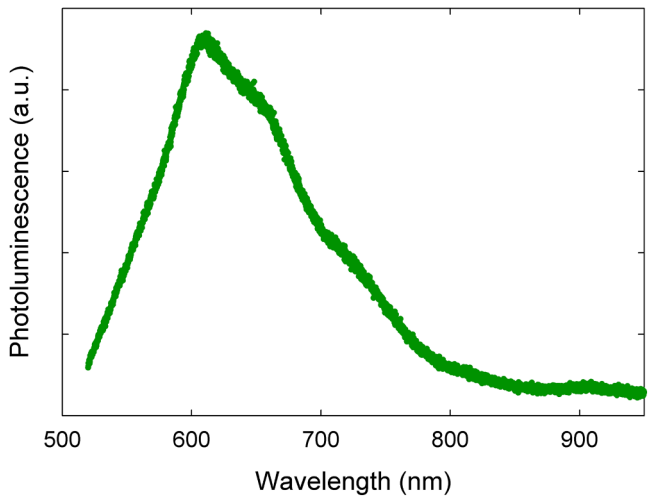

Fig. 8. Photoluminescence spectrum of $Ba_4Sn_4Se_9$.

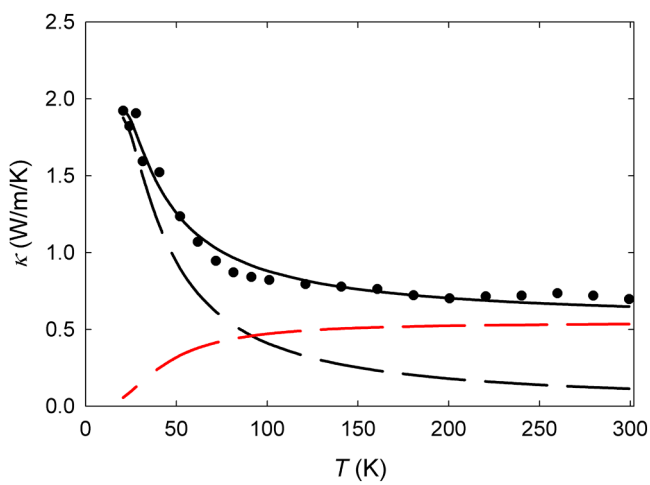

Fig. 9. Temperature dependent κ data. The solid line is a fit to the model described in the text. The contributions from thermal diffusion (red dashed line) as well as the lattice (black dashed line) are shown separately.

be 1.8 using the expression $B \cong \hbar\gamma^2/Mv^2\theta_D$ [71,72]. This relatively high γ value indicates high lattice anharmonicity, the mixed valency also contributing to anharmonicity in $Ba_4Sn_4Se_9$. These findings are corroborated by the low κ values observed for the entire measured temperature range.

4. Conclusions

The crystal structure and physical properties of single crystal $Ba_4Sn_4Se_9$, a new mixed valence composition in the Ba-Sn-Se material system, were investigated. The mixed valency of Sn leads to heterogeneous bonding that, together with a complex crystal structure, directly affects the physical properties. The material possesses a direct band gap of 2.36 eV with very high measured ρ values. Analyses of the temperature dependent κ data using phenomenological models revealed thermal diffusion dominating the thermal transport. A θ_D value of 263 K was obtained using low temperature C_p data. The temperature dependence of C_p/T^3 show deviation from Debye model suggesting the existence of low velocity optic modes corresponding to θ_E of 55 K. The mixed Sn^{2+} and Sn^{4+} cations contribute to the lattice anharmonicity as indicated by a relatively large Gruneisen parameter corroborating the intrinsically low κ for $Ba_4Sn_4Se_9$. Our results and analyses should motivate further investigations into this as well as other compositions in the Ba-Sn-Se system.

CRediT authorship contribution statement

Wilarachchige D.C.B. Gunatilleke: Data curation, Formal analysis, Investigation, Visualization, Writing – original draft. **Winnie Wong-Ng:** Data curation, Validation. **Adam J. Biacchi:** Data curation, Visualization. **Teiyan Chang:** Data curation, Visualization. **Yu-Sheng Chen:** Data curation, Visualization. **George S. Nolas:** Conceptualization, Funding acquisition, Project administration, Supervision, Writing – review & editing.

Declaration of competing interest

The authors declare that they have no known competing financial interests or personal relationships that could have appeared to influence the work reported in this paper.

Data availability

Data will be made available on request.

Acknowledgements

This work was supported, in part, by the National Science Foundation, Grant No. DMR-1748188. The authors acknowledge ChemMatCARS Sector 15 which is principally supported by the National Science Foundation/Department of Energy under grant number NSF/CHE-1834750. Use of the Advanced Photon Source was supported by the U. S. Department of Energy, Office of Science, Office of Basic Energy Sciences, under Contract No. DE-AC02–06CH11357.

Supplementary materials

Supplementary material associated with this article can be found, in the online version, at doi:10.1016/j.actamat.2024.119915.

References

[1] F. Gascoin, A. Maignan, Order–Disorder transition in $AgCrSe_2$: a new route to efficient thermoelectrics, Chem. Mater. 23 (2011) 2510–2513, https://doi.org/10.1021/cm200581k.
[2] U. Aydemir, J.H. Pöhls, H. Zhu, G. Hautier, S. Bajaj, Z.M. Gibbs, W. Chen, G. Li, S. Ohno, D. Broberg, S. Dongmin Kang, M. Asta, G. Ceder, M. Anne White, K. Persson, A. Jain, G. Jeffrey Snyder, $YCuTe_2$: a member of a new class of thermoelectric materials with $CuTe_4$ -based layered structure, J. Mater. Chem. A 4 (2016) 2461–2472, https://doi.org/10.1039/C5TA10330D.
[3] Y. Dong, H. Wang, G.S. Nolas, Synthesis and thermoelectric properties of Cu excess $Cu_2ZnSnSe_4$, Phys. Status Solidi (RRL) Rapid Research Lett. 8 (2014) 61–64, https://doi.org/10.1002/pssr.201308274.
[4] K. Wei, L. Beauchemin, H. Wang, W.D. Porter, J. Martin, G.S. Nolas, Enhanced thermoelectric properties of $Cu_2ZnSnSe_4$ with Ga-doping, J. Alloys. Compd. 650 (2015) 844–847, https://doi.org/10.1016/j.jallcom.2015.08.046.
[5] K. Wei, G.S. Nolas, Synthesis and characterization of nanostructured stannite $Cu_2ZnSnSe_4$ and $Ag_2ZnSnSe_4$ for thermoelectric applications, ACS Appl. Mater. Interfaces 7 (2015) 9752–9757, https://doi.org/10.1021/acsami.5b01617.
[6] R. Vassen, A. Stuke, D. Stöver, Recent developments in the field of thermal barrier coatings, J. Therm. Spray Tech. 18 (2009) 181–186, https://doi.org/10.1007/s11666-009-9312-7.
[7] R.E. Taylor, Thermal conductivity determinations of thermal barrier coatings, Mater. Sci. Eng. A 245 (1998) 160–167, https://doi.org/10.1016/S0921-5093(97)00847-2.
[8] D.R. Clarke, Materials selection guidelines for low thermal conductivity thermal barrier coatings, Surf. Coat. Technol. (2003) 67–74, https://doi.org/10.1016/S0257-8972(02)00593-5, 163–164.
[9] P.G. Klemens, M. Gell, Thermal conductivity of thermal barrier coatings, Mater. Sci. Eng. A 245 (1998) 143–149, https://doi.org/10.1016/S0921-5093(97)00846-0.
[10] G.S. Nolas, M.S. Hassan, Y. Dong, J. Martin, Synthesis, crystal structure and electrical properties of the tetrahedral quaternary chalcogenides CuM_2InTe_4 (M=Zn, Cd), J. Solid. State Chem. 242 (2016) 50–54, https://doi.org/10.1016/j.jssc.2016.03.038.
[11] S.K. Wallace, D.B. Mitzi, A. Walsh, The steady rise of kesterite solar cells, ACS. Energy Lett. 2 (2017) 776–779, https://doi.org/10.1021/acsenergylett.7b00131.

[12] W. Wang, M.T. Winkler, O. Gunawan, T. Gokmen, T.K. Todorov, Y. Zhu, D.B. Mitzi, Device characteristics of CZTSSe thin-film solar cells with 12.6% efficiency, Adv. Energy Mater. 4 (2014) 1301465, https://doi.org/10.1002/aenm.201301465.

[13] S. Palchoudhury, K. Ramasamy, A. Gupta, Multinary copper-based chalcogenide nanocrystal systems from the perspective of device applications, Nanoscale Adv. 2 (2020) 3069–3082, https://doi.org/10.1039/D0NA00399A.

[14] Z. Wang, J. Cai, Q. Wang, S. Wu, J. Li, Unsupervised discovery of thin-film photovoltaic materials from unlabeled data, Npj Comput. Mater. 7 (2021) 1–11, https://doi.org/10.1038/s41524-021-00596-4.

[15] M.E. Maldonado, A. Das, A.M. Jawaid, A.J. Ritter, R.A. Vaia, D.A. Nagaoka, P. G. Vianna, L. Seixas, C.J.S. de Matos, A. Baev, P.N. Prasad, A.S.L. Gomes, Nonlinear Optical Interactions and Relaxation in 2D Layered Transition Metal Dichalcogenides Probed by Optical and Photoacoustic Z-Scan Methods, ACS. Photonics. 7 (2020) 3440–3447, https://doi.org/10.1021/acsphotonics.0c01327.

[16] M.Y. Li, Z. Ma, B. Li, X.T. Wu, H. Lin, Q.L. Zhu, $HgCuPS_4$: an exceptional infrared nonlinear optical material with defect diamond-like structure, Chem. Mater. 32 (2020) 4331–4339, https://doi.org/10.1021/acs.chemmater.0c01258.

[17] I. Chung, M.G. Kanatzidis, Metal Chalcogenides: a Rich Source of Nonlinear Optical Materials, Chem. Mater. 26 (2014) 849–869, https://doi.org/10.1021/cm401737s.

[18] M. Piasecki, G. Myronchuk, O.Y. Khyzhun, A. Fedorchuk, B. Andryievsky, I. Barchyi, M. Brik, Impact of structure complexity on optoelectronic and non-linear optical properties in quaternary Ag(Pb)–Ga(In)–Si(Ge)–S(Se) systems, J. Alloys. Compd. 909 (2022) 164636, https://doi.org/10.1016/j.jallcom.2022.164636.

[19] K. Pal, Y. Xia, J. Shen, J. He, Y. Luo, M.G. Kanatzidis, C. Wolverton, Accelerated discovery of a large family of quaternary chalcogenides with very low lattice thermal conductivity, NPJ. Comput. Mater. 7 (2021) 1–13, https://doi.org/10.1038/s41524-021-00549-x.

[20] W. Lu, R. Xiao, J. Yang, H. Li, W. Zhang, Data mining-aided materials discovery and optimization, J. Materiom. 3 (2017) 191–201, https://doi.org/10.1016/j.jmat.2017.08.003.

[21] W. Liu, Q. Jie, H.S. Kim, Z. Ren, Current progress and future challenges in thermoelectric power generation: from materials to devices, Acta Mater. 87 (2015) 357–376, https://doi.org/10.1016/j.actamat.2014.12.042.

[22] Q. Yan, M.G. Kanatzidis, High-performance thermoelectrics and challenges for practical devices, Nat. Mater. 21 (2022) 503–513, https://doi.org/10.1038/s41563-021-01109-w.

[23] C.M. Varma, Mixed-valence compounds, Rev. Mod. Phys. 48 (1976) 219–238, https://doi.org/10.1103/RevModPhys.48.219.

[24] W. Liu, L. Liu, Y. Wang, L. Chen, J.A. McLeod, L. Yang, J. Zhao, Z. Liu, J. Diwu, Z. Chai, T.E. Albrecht-Schmitt, G. Liu, S. Wang, Tuning mixed-valent Eu^{2+}/Eu^{3+} in strontium formate frameworks for multichannel photoluminescence, Chem. A Euro. J. 22 (2016) 11170–11175, https://doi.org/10.1002/chem.201602621.

[25] F. Ruan, D. Deng, M. Wu, B. Chen, L. Lei, R. Lei, S. Xu, Multichannel luminescence properties and ultrahigh-sensitive optical temperature sensing of mixed-valent Eu^{2+}/Eu^{3+} co-activated $Ca_8ZrMg(PO_4)_6(SiO_4)$ phosphors, J. Alloys. Compd. 784 (2019) 1153–1161, https://doi.org/10.1016/j.jallcom.2019.01.092.

[26] M. Manikandan, T. Tanabe, P. Li, S. Ueda, G.V. Ramesh, R. Kodiyath, J. Wang, T. Hara, A. Dakshanamoorthy, S. Ishihara, K. Ariga, J. Ye, N. Umezawa, H. Abe, Photocatalytic water splitting under visible light by mixed-valence Sn_3O_4, ACS Appl. Mater. Interfaces 6 (2014) 3790–3793, https://doi.org/10.1021/am500157u.

[27] J. Wang, N. Umezawa, H. Hosono, Mixed valence tin oxides as novel van der waals materials: theoretical predictions and potential applications, Adv. Energy Mater. 6 (2016) 1501190, https://doi.org/10.1002/aenm.201501190.

[28] D. Meggiolaro, L. Gregori, F. De Angelis, Formation of a mixed valence Sn_3F_8 phase may explain the SnF_2 stabilizing role in tin-halide perovskites, ACS. Energy Lett. 8 (2023) 2373–2375, https://doi.org/10.1021/acsenergylett.3c00652.

[29] C.J. Krajewska, S.R. Kavanagh, L. Zhang, D.J. Kubicki, K. Dey, K. Gałkowski, C. P. Grey, S.D. Stranks, A. Walsh, D.O. Scanlon, R.G. Palgrave, Enhanced visible light absorption in layered Cs 3 Bi 2 Br 9 through mixed-valence Sn(ii)/Sn(iv) doping, Chem. Sci. 12 (2021) 14686–14699, https://doi.org/10.1039/D1SC03775G.

[30] M.K. Jana, K. Pal, U.V. Waghmare, K. Biswas, The origin of ultralow thermal conductivity in inte: lone-pair-induced anharmonic rattling, Angew. Chem. Int. Ed. 55 (2016) 7792–7796, https://doi.org/10.1002/anie.201511737.

[31] X. Shen, Y. Xia, G. Wang, F. Zhou, V. Ozolins, X. Lu, G. Wang, X. Zhou, High thermoelectric performance in complex phosphides enabled by stereochemically active lone pair electrons, J. Mater. Chem. A 6 (2018) 24877–24884, https://doi.org/10.1039/C8TA08448C.

[32] J. Zhang, D. Ishikawa, M.M. Koza, E. Nishibori, L. Song, A.Q.R. Baron, B.B. Iversen, Dynamic lone pair expression as chemical bonding origin of giant phonon anharmonicity in thermoelectric InTe, Angewandte Chemie 135 (2023) e202218458, https://doi.org/10.1002/ange.202218458.

[33] Y. Dong, A.R. Khabibullin, K. Wei, J.R. Salvador, G.S. Nolas, L.M. Woods, Bournonite $PbCuSbS_3$: stereochemically active lone-pair electrons that induce low thermal conductivity, Chemphyschem. 16 (2015) 3264–3270, https://doi.org/10.1002/cphc.201500476.

[34] Y. Li, L. Wang, Y. Qiao, Y. Gan, D.J. Singh, Prediction of ternary alkaline-earth metal Sn(II) and Pb(II) chalcogenide semiconductors, Phys. Rev. Mater. 4 (2020) 055004, https://doi.org/10.1103/PhysRevMaterials.4.055004.

[35] M. Zelinska, A. Assoud, C. Graf, H. Kleinke, Reversible Reconstructive phase transition of ba_2snse_5: a new high temperature modification with completely different structural motifs, Inorg. Chem 49 (2010) 1090–1093, https://doi.org/10.1021/ic901989j.

[36] K. Feng, X. Jiang, L. Kang, W. Yin, W. Hao, Z. Lin, J. Yao, Y. Wu, C. Chen, $Ba_6Sn_6Se_{13}$: a new mixed valence selenostannate with NLO property, Dalton Transactions 42 (2013) 13635–13641, https://doi.org/10.1039/C3DT51317C.

[37] A. Assoud, N. Soheilnia, H. Kleinke, The new semiconducting polychalcogenide Ba_2SnSe_5 exhibiting Se_{32}- units and distorted $SnSe_6$ octahedra, J. Solid. State Chem. 178 (2005) 1087–1093, https://doi.org/10.1016/j.jssc.2005.01.011.

[38] A. Assoud, H. Kleinke, Unique Barium Selenostannate−Selenide: $Ba_7Sn_3Se_{13}$ (and Its Variants $Ba_7Sn_3Se_{13-\delta}Te_\delta$) with $SnSe_4$ Tetrahedra and Isolated Se Anions, Chem. Mater. 17 (2005) 4509–4513, https://doi.org/10.1021/cm050787y.

[39] K. Wu, X. Su, Z. Yang, S. Pan, An investigation of new infrared nonlinear optical material: $baCdSnSe_4$, and three new related centrosymmetric compounds: ba_2SnSe_4, Mg_2GeSe_4, and $Ba_2Ge_2S_6$, Dalton Trans. 44 (2015) 19856–19864, https://doi.org/10.1039/C5DT03215F.

[40] G. Tan, L.D. Zhao, M.G. Kanatzidis, Rationally designing high-performance bulk thermoelectric materials, Chem. Rev. 116 (2016) 12123–12149, https://doi.org/10.1021/acs.chemrev.6b00255.

[41] G.M. Sheldrick, SHELXT – Integrated space-group and crystal-structure determination, Acta Cryst A 71 (2015) 3–8, https://doi.org/10.1107/S2053273314026370.

[42] G.M. Sheldrick, A short history of SHELX, Acta Cryst A 64 (2008) 112–122, https://doi.org/10.1107/S0108767307043930.

[43] P. Giannozzi, S. Baroni, N. Bonini, M. Calandra, R. Car, C. Cavazzoni, D. Ceresoli, G.L. Chiarotti, M. Cococcioni, I. Dabo, A.D. Corso, S. de Gironcoli, S. Fabris, G. Fratesi, R. Gebauer, U. Gerstmann, C. Gougoussis, A. Kokalj, M. Lazzeri, L. Martin-Samos, N. Marzari, F. Mauri, R. Mazzarello, S. Paolini, A. Pasquarello, L. Paulatto, C. Sbraccia, S. Scandolo, G. Sclauzero, A.P. Seitsonen, A. Smogunov, P. Umari, R.M. Wentzcovitch, QUANTUM ESPRESSO: a modular and open-source software project for quantum simulations of materials, J. Phys.: Condens. Matter 21 (2009) 395502, https://doi.org/10.1088/0953-8984/21/39/395502.

[44] J.P. Perdew, K. Burke, M. Ernzerhof, Generalized gradient approximation made simple, Phys. Rev. Lett. 77 (1996) 3865–3868, https://doi.org/10.1103/PhysRevLett.77.3865.

[45] J.P. Perdew, M. Ernzerhof, K. Burke, Rationale for mixing exact exchange with density functional approximations, J. Chem. Phys. 105 (1996) 9982–9985, https://doi.org/10.1063/1.472933.

[46] P.E. Blöchl, O. Jepsen, O.K. Andersen, Improved tetrahedron method for Brillouin-zone integrations, Phys. Rev. B 49 (1994) 16223–16233, https://doi.org/10.1103/PhysRevB.49.16223.

[47] K. Momma, F. Izumi, VESTA: a three-dimensional visualization system for electronic and structural analysis, J Appl Cryst 41 (2008) 653–658, https://doi.org/10.1107/S0021889808012016.

[48] J. Martin, G.S. Nolas, Apparatus for the measurement of electrical resistivity, Seebeck coefficient, and thermal conductivity of thermoelectric materials between 300K and 12K, Rev. Sci. Inst. 87 (2016) 015105, https://doi.org/10.1063/1.4939555.

[49] J. Martin, S. Erickson, G.S. Nolas, P. Alboni, T.M. Tritt, J. Yang, Structural and transport properties of $Ba_8Ga_{16}Si_xGe_{30-x}$ clathrates, J. Appl. Phys. 99 (2006) 044903, https://doi.org/10.1063/1.2171775.

[50] S. Stefanoski, J. Martin, G.S. Nolas, Low temperature transport properties and heat capacity of single-crystal Na_8Si_{46}, J. Phys. Condens. Matter 22 (2010) 485404, https://doi.org/10.1088/0953-8984/22/48/485404.

[51] M. Beekman, W. Schnelle, H. Borrmann, M. Baitinger, Yu. Grin, G.S. Nolas, Intrinsic Electrical and Thermal Properties from Single Crystals of $Na_{24}Si_{136}$, Phys. Rev. Lett. 104 (2010) 018301, https://doi.org/10.1103/PhysRevLett.104.018301.

[52] W.D.C.B. Gunatilleke, W. Wong-Ng, T. Chang, Y.S. Chen, G.S. Nolas, Structure, electrical and thermal properties of single-crystal $BaCuGdTe_3$, Dalton Transactions 52 (2023) 8316–8321, https://doi.org/10.1039/D3DT01192E.

[53] W.D.C.B. Gunatilleke, K. Wei, Z. Niu, L. Wojtas, G. Nolas, S. Ma, Thermal conductivity of a perovskite-type metal–organic framework crystal, Dalton Transactions 46 (2017) 13342–13344, https://doi.org/10.1039/C7DT02927F.

[54] J. Yao, W. Yin, K. Feng, X. Li, D. Mei, Q. Lu, Y. Ni, Z. Zhang, Z. Hu, Y. Wu, Growth and characterization of $BaGa_4Se_7$ crystal, J. Cryst. Growth 346 (2012) 1–4, https://doi.org/10.1016/j.jcrysgro.2012.02.035.

[55] O. Hellman, D.A. Broido, Phonon thermal transport in Bi_2Te_3 from first principles, Phys. Rev. B 90 (2014) 134309, https://doi.org/10.1103/PhysRevB.90.134309.

[56] Z.Y. Dong, Y. Zhou, X.Q. Chen, W.J. Li, Z.Y. Cao, C. Luo, G.H. Zhong, Q. Peng, X. Wu, X.J. Chen, Effect of low-frequency optical phonons on the thermal conductivity of ^2H molybdenum disulfide, Phys. Rev. B 105 (2022) 184301, https://doi.org/10.1103/PhysRevB.105.184301.

[57] H. Liu, J. Yang, X. Shi, S.A. Danilkin, D. Yu, C. Wang, W. Zhang, L. Chen, Reduction of thermal conductivity by low energy multi-Einstein optic modes, J. Materiom. 2 (2016) 187–195, https://doi.org/10.1016/j.jmat.2016.05.006.

[58] C. Kittel, P. McEuen, Introduction to Solid State Physics, John Wiley & Sons, 2018.

[59] E. Gopal, Specific Heats at Low Temperatures, Springer Science & Business Media, 2012.

[60] M. Beekman, R.P. Hermann, A. Möchel, F. Juranyi, G.S. Nolas, A study of low-energy guest phonon modes in clathrate-II Na_xSi_{136} (x = 3, 23, and 24), J. Phys. Condens. Matter 22 (2010) 355401, https://doi.org/10.1088/0953-8984/22/35/355401.

[61] S. Stefanoski, C.D. Malliakas, M.G. Kanatzidis, G.S. Nolas, Synthesis and structural characterization of Na_xSi_{136} ($0 < x \leq 24$) single crystals and low-temperature transport of polycrystalline specimens, Inorg. Chem. 51 (2012) 8686–8692, https://doi.org/10.1021/ic202199t.

[62] G.S. Nolas, G. Fowler, J. Yang, Assessing the role of filler atoms on the thermal conductivity of filled skutterudites, J. Appl. Phys. 100 (2006) 043705, https://doi.org/10.1063/1.2245204.

[63] W.D.C.B. Gunatilleke, R. Juneja, O.P. Ojo, A.F. May, H. Wang, L. Lindsay, G. S. Nolas, Intrinsic anharmonicity and thermal properties of ultralow thermal conductivity $Ba_6Sn_6Se_{13}$, Phys. Rev. Mater. 5 (2021) 085002, https://doi.org/10.1103/PhysRevMaterials.5.085002.

[64] E. Bauer, H. Kaldarar, R. Lackner, H. Michor, W. Steiner, E.W. Scheidt, A. Galatanu, F. Marabelli, T. Wazumi, K. Kumagai, M. Feuerbacher, Superconductivity in the complex metallic alloy beta-Al_3Mg_2, Phys. Rev. B 76 (2007) 014528, https://doi.org/10.1103/PhysRevB.76.014528.

[65] P.B. Allen, J.L. Feldman, Thermal conductivity of disordered harmonic solids, Phys. Rev. B 48 (1993) 12581–12588, https://doi.org/10.1103/PhysRevB.48.12581.

[66] P.B. Allen, J.L. Feldman, J. Fabian, F. Wooten, Diffusons, locons and propagons: character of atomie yibrations in amorphous Si, Philos. Magaz. B 79 (1999) 1715–1731, https://doi.org/10.1080/13642819908223054.

[67] T. Bernges, R. Hanus, B. Wankmiller, K. Imasato, S. Lin, M. Ghidiu, M. Gerlitz, M. Peterlechner, S. Graham, G. Hautier, Y. Pei, M.R. Hansen, G. Wilde, G.J. Snyder, J. George, M.T. Agne, W.G. Zeier, Considering the role of ion transport in diffuson-dominated thermal conductivity, Adv. Energy Mater. 12 (2022) 2200717, https://doi.org/10.1002/aenm.202200717.

[68] M.K. Gupta, J. Ding, D. Bansal, D.L. Abernathy, G. Ehlers, N.C. Osti, W.G. Zeier, O. Delaire, Strongly anharmonic phonons and their role in superionic diffusion and ultralow thermal conductivity of Cu_7PSe_6, Adv. Energy Mater. 12 (2022) 2200596, https://doi.org/10.1002/aenm.202200596.

[69] J. Callaway, Model for lattice thermal conductivity at low temperatures, Phys. Rev. 113 (1959) 1046–1051, https://doi.org/10.1103/PhysRev.113.1046.

[70] M.T. Agne, R. Hanus, G.Jeffrey Snyder, Minimum thermal conductivity in the context of diffuson -mediated thermal transport, Energy Environ. Sci. 11 (2018) 609–616, https://doi.org/10.1039/C7EE03256K.

[71] D.T. Morelli, G.A. Slack, S.L. Shindé, J.S. Goela, High Lattice Thermal Conductivity Solids. High Thermal Conductivity Materials, Eds., Springer, New York, NY, 2006, pp. 37–68, https://doi.org/10.1007/0-387-25100-6_2.

[72] G.A. Slack, H. Ehrenreich, F. Seitz, D. Turnbull, The Thermal Conductivity of Nonmetallic Crystals. Solid State Physics, Eds., Academic Press, 1979, pp. 1–71, https://doi.org/10.1016/S0081-1947(08)60359-8.